

Multi-waveband polarimetric observations of NRAO 530 on parsec-scale

Y. J. Chen^{1*}, Z.-Q. Shen¹ and S.-W. Feng²

¹*Key Laboratory for Research in Galaxies and Cosmology, Shanghai Astronomical Observatory, Chinese Academy of Sciences, Shanghai 200030, P.R. China*

²*Department of Space Science and Applied Physics, Shandong University at Weihai, Weihai 264209, China*

Accepted 2010 June 12. Received 2010 June 11; in original form 2009 October 18

ABSTRACT

We report on VLBA polarimetric observations of NRAO 530 at 5, 8, 15, 22, and 43 GHz within an interval of one week in February 1997. Total intensity, fractional polarization and electric vector position angle (EVPA) distributions at all these frequencies are presented. Model fitting has been performed to the full polarization visibility data, from which the fitted southmost component *A* is confirmed as the core of the radio structure with relatively high brightness temperature and hard spectrum between 15 and 43 GHz in comparison with the central component *B* of dominant flux. The relatively high degree of polarization for the component *A* may arise from its complex radio structure, which is resolvable at 86 GHz. As a contrast, the component *B* shows a well fitted power-law spectrum with the spectral index of about -0.5 ($f \propto \nu^\alpha$), and a linear correlation between EVPAs and wavelength square with the observed rotation measure (RM) of about -1062 rad m^{-2} , indicating its structural singleness. Assuming that the component *B* has a comparable degree of polarization without depolarization at these frequencies, the decrease in fractional polarization with wavelength mainly results from opacity and Faraday rotation, in which the opacity plays quite a large part of role. A spine-sheath like structure in fractional polarization (*m*) is detected covering almost the whole emission region at 5 and 8 GHz, with degree of polarization relatively low along the jet spine, and getting higher toward two sides of the jet. The linear polarization at 5 GHz shows 3 separate polarized emission regions with alternately aligned and orthogonal polarization vectors down the jet. The polarization goes to zero between the top two regions, with the highest polarization level occurring at the top and bottom. The 5 and 8 GHz images show EVPA changes across the width of the jet as well as along the jet. These complex polarimetric properties can be explained in terms of either the presence of a large helical magnetic field or tangled magnetic fields compressed and sheared down the jet, which can be further determined by multi-frequency polarimetric VLBI observation with sufficient high resolution and sensitivity spanning over an appropriate frequency range.

Key words: galaxies: active – galaxies: jets – polarization – quasars: individual (NRAO 530) – radio continuum: galaxies

1 INTRODUCTION

In the leading model for jet production, acceleration, and collimation in blazars, magnetic field plays an important role (e.g. Meier, Koide & Uchida 2001; McKinney 2006). The poloidal magnetic fields are supposed to be wound up by the differential rotation of a rotating disk or ergosphere surrounding a central supermassive black hole, propagating outward in the polar directions with a tight

helical pattern. On pc scale or beyond the jet acceleration region, the magnetic fields within jet might maintain a tight helical pattern (Lyutikov, Pariev & Gabuzda 2005), become chaotic, or possibly get compressed and sheared (Jorstad et al. 2007). The degree of order and geometry of the magnetic field will differ from case to case, and therefore can help to better understand the physical conditions in a jet.

Since the jet emission is mainly synchrotron radiative, and hence linearly polarized with electric vector perpendicular to the projection on the sky of the magnetic field

* E-mail: cyj@shao.ac.cn

(Begelman, Blandford & Rees 1984), the magnetic geometry and order of degree can be revealed to some degree through polarimetric Very Long Baseline Interferometry (VLBI) observation. The dominant transverse magnetic field is often ascribed to shock compression, and the dominant longitudinal one to the effect of shear or interaction with surrounding medium (e.g. Laing 1980; Hughes, Aller & Aller 1989). However, both cases can also be interpreted in terms of intrinsic helical magnetic fields, which appear more natural and simpler (e.g. Gabuzda, Murray & Cronin 2004). It is difficult to distinguish between transverse magnetic fields due to a toroidal field component and due to shock compression. Under the circumstances, the measurement of RM gradient across the jet is proposed to test the magnetic helicity within or wrapping around the jet (Blandford 1993), which has been detected in some sources such as 3C 273 (Asada et al. 2002; Zavala & Taylor 2005) through multi-band polarimetric VLBI observation with sufficiently good visibility data.

As a typical blazar, NRAO 530 (J1733-1304) is strong and variable in almost the whole wave bands from radio to γ -ray. Long term monitoring at cm wavelengths from 1967 to 2003 shows a bright outburst peaking around 1997 (Pyatunina et al. 2006), which is almost coincident with our VLBI observations. In this paper, we present the polarimetric VLBI observational results of NRAO 530 at 5 frequencies. Model fitting has been done to the full polarization data, with the physical properties of the southmost component *A* and the central component *B* analyzed and discussed in more detail. Since the total intensity structures have been reported in Feng et al. (2006), we here focus more on the polarimetric properties of the source on parsec scale.

In §2 we present the whole process of data reduction. Results are shown in §3, followed by discussions in §4. A summary is given in §5. Throughout this paper, we take the cosmological parameters of $H_0 = 71 \text{ km s}^{-1} \text{ Mpc}^{-1}$, $\Omega_M = 0.27$, and $\Omega_\Lambda = 0.73$ in calculating angular distance, with 1 mas of angular size corresponding to 7.8 pc for NRAO 530 with a redshift of 0.902.

2 OBSERVATIONS AND DATA REDUCTION

We observed NRAO 530 at 5, 8, 15, 22, and 43 GHz in February 1997 with Very Long Baseline Array (VLBA) plus one VLA antenna. Three separate observations were made within an interval of 7 days, with the first observation at 5 and 8 GHz made on February 7, the second one at 15 and 22 GHz on February 12, and the third at 43 GHz on February 14. Some other specific observational information can be found in Feng et al. (2006). Based on the UMRAO data during the observational period, the largest flux density variation at 5, 8, and 15 GHz is about 4%, and the observations at 15, 22, and 43 GHz were made within an interval of 2 days, whose total flux density available at 15 GHz almost kept constant within the observational error of about 2% from February 8 to 10. This means that a 2 day interval of observations almost has no impact on the following analysis of the resultant spectral indices and RMs derived from the high 3 frequency observations.

The data reduction and imaging were done in the AIPS and DIFMAP packages respectively by using standard tech-

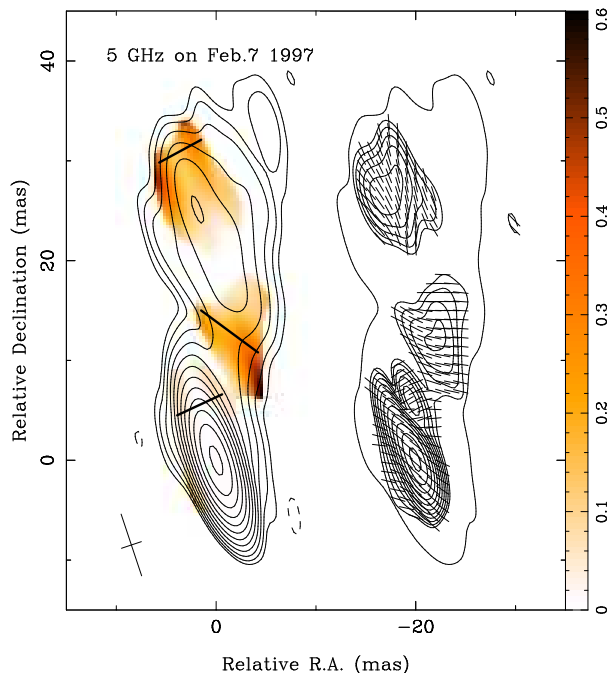
niques, as described in Zavala & Taylor (2004). Careful data editing was first done to flag out those obviously bad data points, including all the visibility data to antenna MK at 5 and 8 GHz, and those visibilities to BR at 15 and 22 GHz due to failure of correlation, and some other points due to the too low elevation angle. Standard amplitude and phase calibration were performed subsequently. Here, we'd like to stress that we make antenna gain(s) calibration with 'CLCOR' to one or more antennas in AIPS before imaging because at least one antenna gain is required to be adjusted at all but 43 GHz.

NRAO 530 was observed as a calibrator during the observations. It is very strong and compact, and hence the fringes can be easily detected on almost all the baselines. Due to its relatively complex radio structure, the task 'CCEDT' in AIPS was used to separate the total intensity distribution into several point sources by hand to calibrate the instrumental polarization ('D-terms') of each antenna with the AIPS task 'LPCAL'. To ensure that the D-terms solutions were acceptable, we checked the distribution of the normalized cross visibilities in complex (real and imaginary) plane, with and without instrumental calibration. We found that it gets well clustered after the instrumental calibration is made. An additional effort is also tried to obtain an independent set of D-terms from another calibrator OV-236, which was observed for about half of the on-source time on NRAO 530. These solutions are quite consistent at 5 and 8 GHz. At 15 GHz and higher frequencies, there are some differences. The distribution of the normalized visibilities in complex plane gets better clustered, and the final results have a better dynamic range, especially at 15 and 22 GHz when using the D-terms from NRAO 530 alone. Therefore, in this paper, we adopted the D-terms solutions derived from NRAO 530 alone.

The absolute EVPA calibrations at 5, 8, and 15 GHz were performed by using the integral EVPA within 5 days of our observations from Radio Astronomy Observatory Database at University of Michigan (UMRAO) (cf. Aller et al. 1985). The absolute EVPAs are $52.8^\circ \pm 2.7^\circ$ at 5.0 GHz, $73.4^\circ \pm 2.2^\circ$ at 8.0 GHz, and $70.8^\circ \pm 2.0^\circ$ at 15.4 GHz, respectively. At 22 and 43 GHz no absolute EVPAs are available, thus the true EVPAs at the two frequencies are estimated by using RM of about -109 rad m^{-2} obtained at lower frequencies. The resultant values at the two frequencies are about 75.5° and 76.6° , respectively. Corrections to EVPA are obtained by doubling the difference between the integral EVPA from UMRAO and the observed integral EVPA at each frequency, and then applied to the visibility data with the AIPS task 'CLCOR'. In comparison to the UMRAO data, about 83%, 86% and 76% of polarized flux at 5, 8 and 15 GHz get recovered respectively in our observations, that is to say that the adopted EVPA corrections is roughly reasonable with the corresponding uncertainties of 0.4° , 2.2° and 0.3° due to the missing flux. Table 1 lists the reference antenna and corresponding EVPA correction at each frequency. The final images, including the total intensity, fractional polarization, linear intensity and EVPA distributions are shown in Figures 1 and 2, which are analyzed and discussed in §3 and §4, respectively.

Table 1. Reference antenna and corresponding EVPA correction at each frequency

Obs. Freq. (GHz)	5	8	15	22	43
Ref. Antenna	FD	FD	PT	PT	LA
χ (deg)	-33.6	156.6	-16.4	19.1	77.6

**Figure 1.** VLBI polarimetric image of NRAO 530 at 5 GHz. Left: fractional linear polarization image (color) overlaid by total intensity contours. The restoring beam has dimensions of $6.5 \text{ mas} \times 2.1 \text{ mas}$ at position angle 18.4° , indicated at the bottom left corner. Contours start at $2.9 \text{ mJy beam}^{-1}$ and increase by factors of 2. The thick lines indicate the location of the slices shown in Figure 5. Right: EVPA distribution of NRAO 530 with contours of polarimetric intensity overlaid. Contours start at $2.4 \text{ mJy beam}^{-1}$ and increase by a factor $\sqrt{2}$ for linearly polarized intensity contours.

3 RESULTS

3.1 Total intensity distribution and model fitting to the full visibility data

The results and analysis of the total intensity distributions have been presented in Feng et al. (2006), where spectral fits to some of the components and radiative mechanism are investigated in detail. Here, we reproduce the intensity distributions at all the 5 frequencies as contour profiles in the left panel of each map in Figures 1 and 2, with antenna gains calibrated to those antennas of unreasonable magnitude by checking amplitude versus distance plots at all but 43 GHz before imaging this time (e.g. Zavala & Taylor 2004). This gives rise to small differences in the resultant components' amplitude in model fitting. In terms of the recovered proportion of total flux density on pc scale, the current results are more consistent in comparison to that shown in MOJAVE data archive (<http://www.physics.purdue.edu/astro/mojave>). The total

intensity distributions show that the detectable emission region decreases rapidly with frequency. This is mainly due to large changes in resolution, and the sensitivity difference at different frequencies may also have contribution to it.

Model fitting is done using the MODELFIT program in the DIFMAP package. Since a model fit to total intensity distribution is not necessarily unique (Lister et al. 2009), we tried not to introduce any artificial estimate into the process of model fitting to keep the same components as presented in Feng et al. (2006). We started with a Gaussian component to model the Stokes I structure. When the reduced Chi-square no longer decreases and there are still sufficient bright feature(s) present in the residual image, a new Gaussian component is added into the residual image for further fitting. The process was repeated until no apparently bright feature could be found in the residual image. The linear polarization is fitted using the same components as derived from the total intensity fits with the only parameter flux left free to estimate the Stokes Q and U flux density, and the corresponding linear polarized flux and positional angle were obtained by using $P = \sqrt{Q^2 + U^2}$ and $\chi = 0.5 \arctan U/Q$, respectively.

The fitting results of the southmost component A and the component B at phase tracking center (hereafter central component) (see the right bottom panel of Figure 2) are shown in Table 2, where flux density (f_ν), fractional polarization (m), EVPA, major axis (θ_{maj}), axial ratio ($\theta_{maj}/\theta_{min}$) and the derived brightness temperature (T_B) in the source frame for both components are listed in the corresponding columns. The T_B is estimated by using the following expression (Ghisellini et al. 1993),

$$T_B = 1.77 \times 10^{12} \left(\frac{f_\nu}{\text{Jy}} \right) \left(\frac{\nu}{\text{GHz}} \right)^{-2} \left(\frac{\theta_d}{\text{mas}} \right)^{-2} (1+z), \quad (1)$$

where f_ν is flux density at frequency ν , θ_d is angular size $\theta_d = \sqrt{\theta_{maj}\theta_{min}}$ with θ_{maj} and θ_{min} being major and minor axis, respectively. Due to large difference in resolutions, we cannot separate the southmost component A at lower frequencies 5 and 8 GHz, the central component B at the two frequencies therefore probably contains a larger emission region in comparison to that at higher frequencies, and will be investigated separately from the other frequencies below.

The total intensity distributions show a typical core-jet structure with jet roughly extending to north. Small fluctuations of jet orientation occurs down the jet, which can be more clearly seen by comparing radio structures at different frequencies. One can find in Table 2 that the component A lies in the extreme end of the radio structure, and has relatively high brightness temperature in comparison to the component B , although its flux density is relatively low. This may imply that it is the component A that represents the radio core of the source. To have more evidence for the hypothesis, we fitted power law spectra to both components from 15 GHz to 43 GHz, which is shown in Figure 3. The spectral indices for component A and B are estimated to be 0.08 ± 0.11 and -0.52 ± 0.03 , respectively. Obviously, the power-law spectrum for component A is fitted badly, but surely harder, while the component B exhibits a spectrum of quite a good power-law form, which argues for the core hypothesis of the component A , as suggested in Jorstad et al. (2001) and Feng et al. (2006).

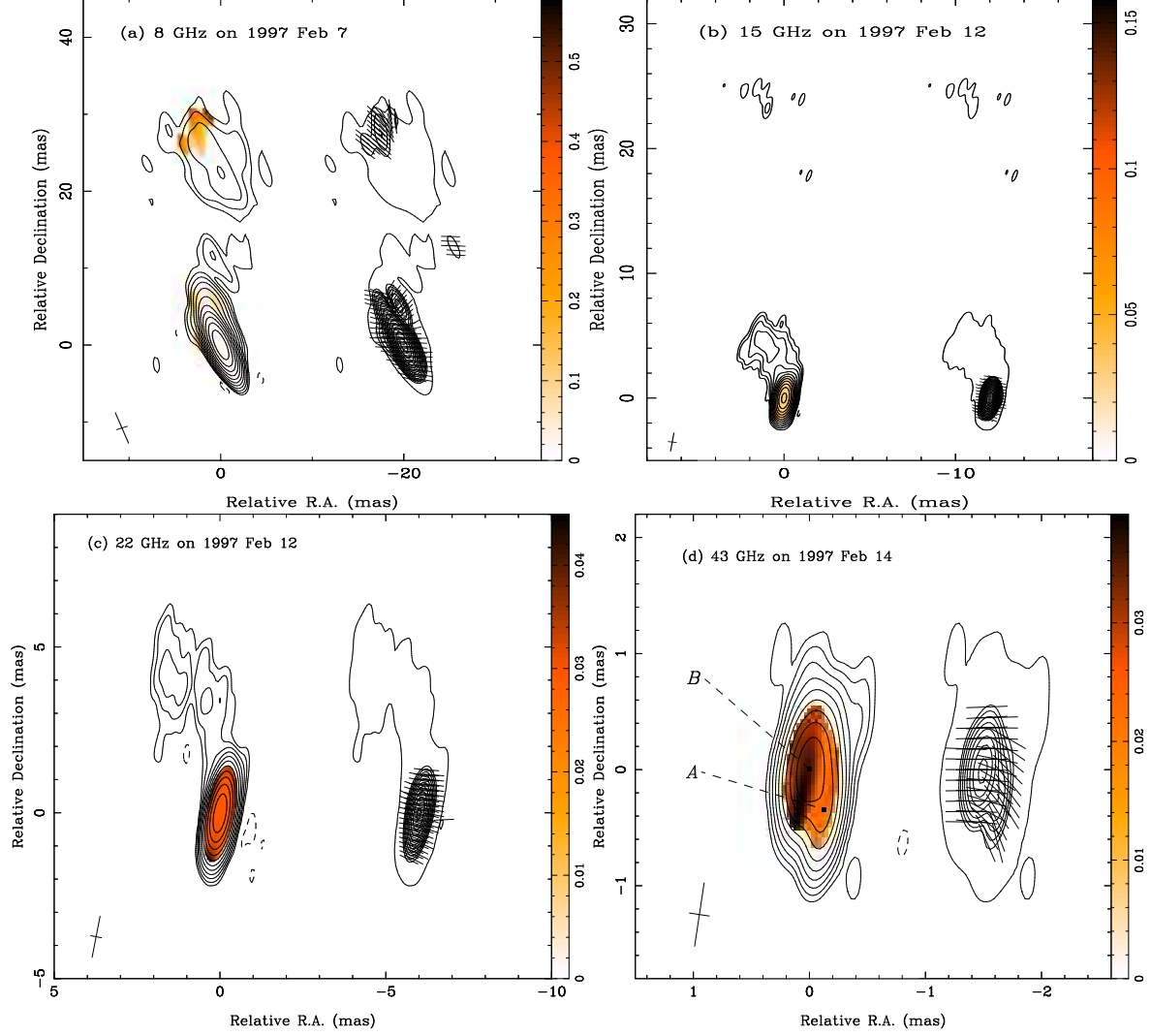


Figure 2. The same as that in Fig. 1, but at four different frequencies: (a) 8 GHz, (b) 15 GHz, (c) 22 GHz, and (d) 43 GHz. (a): the restoring beam is $4.2 \text{ mas} \times 1.2 \text{ mas}$ at 20.0° , contours start at $5.3 \text{ mJy beam}^{-1}$ for total intensity and $2.8 \text{ mJy beam}^{-1}$ for linearly polarized intensity. (b): the restoring beam is $1.5 \text{ mas} \times 0.5 \text{ mas}$ at -7.7° , contours start at $3.5 \text{ mJy beam}^{-1}$ for total intensity and $6.0 \text{ mJy beam}^{-1}$ for linearly polarized intensity. (c): the restoring beam is $1.3 \text{ mas} \times 0.3 \text{ mas}$ at -10.9° , contours start at $4.2 \text{ mJy beam}^{-1}$ for total intensity and $9.5 \text{ mJy beam}^{-1}$ for linearly polarized intensity. (d): the restoring beam is $0.55 \text{ mas} \times 0.17 \text{ mas}$ at -8.6° , contours start at $7.5 \text{ mJy beam}^{-1}$ for total intensity and $10.5 \text{ mJy beam}^{-1}$ for linearly polarized intensity. *A* and *B* indicates the location of the fitted Gaussian components *A* and *B* listed in Table 2.

Table 2. Model parameters to components *A* and *B*

Component ID	Freq. (GHz)	f_ν (Jy)	m (%)	χ (deg)	θ_{maj} (mas)	$\theta_{min}/\theta_{maj}$	T_B (10^{12} K)
<i>A</i>	15	1.01	4.97	49.9	0.046	1.0	6.86
	22	1.74	5.45	56.0	0.052	1.0	4.30
	43	1.30	5.22	21.8	0.035	1.0	1.87
<i>B</i>	5*	6.85	1.32	48.6	1.032	0.291	2.99
	8*	9.76	2.01	73.9	0.615	0.214	5.73
	15	8.49	2.95	71.6	0.184	0.586	6.11
	22	7.30	3.13	83.7	0.269	0.467	1.47
	43	4.86	4.46	91.8	0.169	0.893	0.34

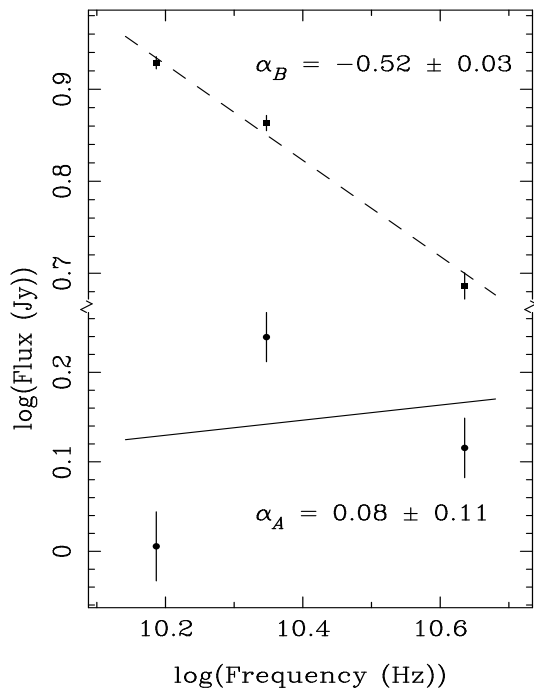


Figure 3. Power-law spectral fitting to components *A* (solid line) and *B* (dashed line) from 15 GHz to 43 GHz.

3.2 Fractional polarization distribution

The polarization imaging results are shown in Figures 1 and 2, with fractional polarization superposed by the total intensity contours, and the EVPA structure superposed by linearly polarized intensity contours at all the 5 frequencies. The 5 GHz imaging result is shown alone for more discussions later. At this frequency, the total and polarized intensity distribution have a much better sensitivity in comparison with that at other frequencies (see captions in Figures 1 and 2). The lowest contours for total and linearly polarized intensity distribution are over 3 times the noise level ($\geq 3\sigma$) at all the 5 frequencies. The emission region with detectable linear polarization decreases gradually in size from 30 mas to a few mas with increasing observational frequency due to increasing resolution and lower surface brightness of the more distant emission, making this emission much harder to detect at high frequency.

As is shown in these images, the fractional polarization distribution at all the 5 frequencies shows an overall tendency of increase in degree of polarization with frequency. Such a frequency dependent fractional polarization can be more clearly seen in Table 2, where the degree of polarization for the component *A* available at 15, 22 and 43 GHz and *B* at all 5 frequencies are listed. The two components contain most of polarized emission of the whole source, and hence may represent such a dependence of polarization level on frequency. The overall fractional polarization from low to high frequency is 1.6%, 2.3%, 2.9%, 3.7% and 2.9%, respectively. At 43 GHz, the overall degree of polarization is a little lower than that at 22 GHz. This may mainly be due to the fact that the available radio structure at 43 GHz mostly lies in a region closer to the core, where there exists more considerable substructures, and the opacity and Faraday depolarization are more severe, thus dragging down the

overall polarization level (e.g. Taylor 1998). And the overall dependence of polarization level on frequency is probably because that at lower frequency, the depolarization by Faraday rotation is more severe, and the resolution is relatively low.

In the outmost region of the 5 and 8 GHz fractional polarization, there exists a prominent blob with extremely high fractional polarization. In contrast, the core region shows a lower polarization level although the absolute linear intensity is relatively strong at all the 5 frequencies. The relatively low polarization level in the core region in comparison with that in jet is also observed in many other sources such as 3C 273, 3C 279, 1803+784, etc, which may well be due to large opacity effect, considerable substructures in the core region, and/or plasma in the immediate vicinity of the AGN (e.g. Taylor 1998; Homan et al. 2009).

3.2.1 Transverse fractional polarization

One may notice that in Figure 1, the fractional polarization at 5 GHz is relatively low along the local jet spine, but gets higher toward the jet edges beyond ~ 5 mas from the core region (referred to as spine-sheath like structure hereafter). At 8 GHz, although it is not so obvious, one can still find such a signature at about 5 and 25 mas from the core, the only two regions with polarization information available, while at 15, 22, and 43 GHz, it is difficult to make sure that this feature exists for the current data. To have quantitative idea on polarization level across the jet, three slices perpendicular to local jet direction are selected for *m* profiles, with the local jet direction defined to be that pointing from one component to the next down the jet at 5 GHz. The fitted component distribution at 5 GHz is shown in Figure 4, with each component indicated as an elliptical form by the fitted position, size and orientation. One can find that the radio structure is well reproduced with these components. In the core region containing 4 fitted components, we cannot definitely determine the local jet direction according to the component distribution, and choose the component's moving direction with positional angle (P.A.) of 25° as the local jet direction from Lister et al. (2009). The selected slices lie in 3 separate regions of detectable polarization emission with P.A. of 115° , 54° and 118° from south to north, as is indicated in Figure 1. The *m* profiles on these slices are shown in Figure 5, displaying that the polarization level is relatively low in the jet spine, but gets higher towards both sides of the jet. If we ignore the patch of extremely high fractional polarization at the right bottom of the middle region, this trend would appear a bit more remarkable.

3.3 Projected polarization structure and Faraday rotation

The projected polarization structure throughout the 5 frequencies are shown in the right panel of each map in Figures 1 and 2, where the linearly polarized intensity distribution is superposed. As can be seen in all these images, the electric field is locally well-ordered from the core to the outmost emission region. For the 5 GHz polarization image with high signal to noise ratio, the electric field information can be well extracted on a scale of more than 30 mas from the core, corresponding to a linear size of 240 pc. At this frequency, the

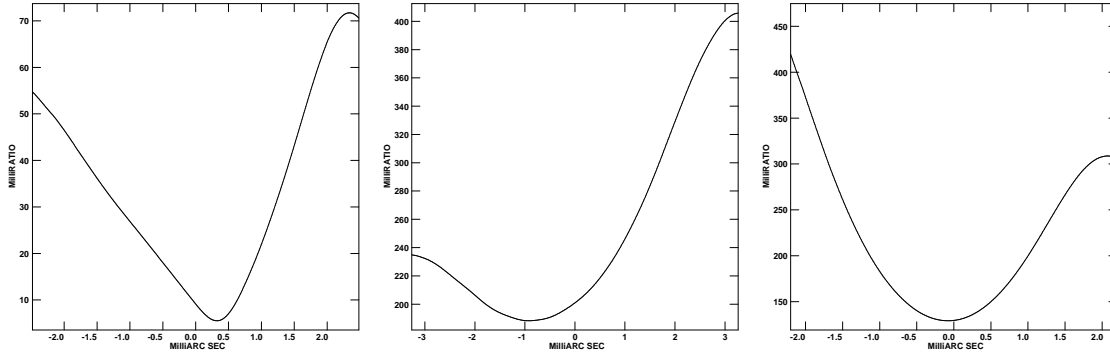


Figure 5. The 5 GHz m profiles across the jet on slices: (a) in the bottom region with P.A. of 115° , (b) in the middle region with P.A. of 54° , (c) in the top region with P.A. of 118° , as indicated in Figure 1.

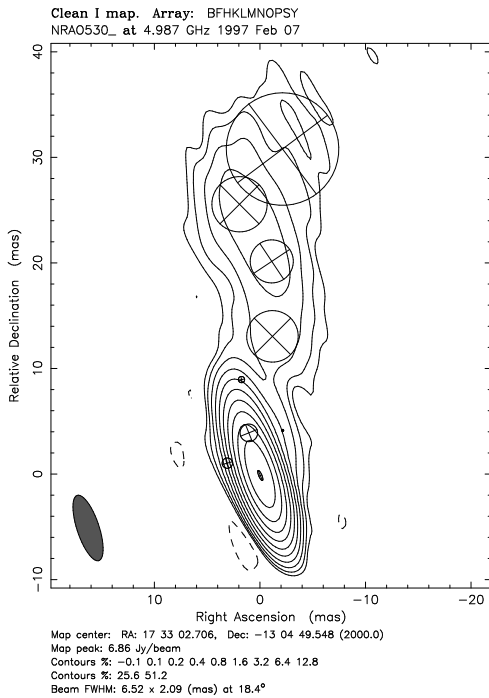


Figure 4. Model fit to the total intensity visibilities at 5 GHz. Each component is represented in an elliptic form with the fitted position, size and orientation.

electric vector is distributed with P.A. of about 50° near the core, and then bifurcate apparently at a distance of about 5 mas north to the core (see also the polarization image at 8 GHz). When the jet reaches a distance of about 10 mas from the core, the electric field turns almost perpendicular to the overall jet direction with an overall P.A. of $\sim 78^\circ$. At a distance of about 25 mas north to the core, the electric vector becomes roughly parallel to the north direction with an overall P.A. of $\sim 23^\circ$. Such an orientation change down the jet may be attributed to magnetic fields that are ordered by local phenomena at various places in the jet, while Gabuzda, Murray & Cronin (2004) suggested that these alternating magnetic fields may indicate oscillations or instabilities of a global jet magnetic field.

Faraday rotation reveals some physical condition along the line of sight. When the polarized emission propagates through a magnetized plasma, the polarization plane will

rotates with wavelength λ according to the following expression (e.g. Taylor 1998),

$$\Delta\chi = 812\lambda^2 \int N(\mathbf{s})\mathbf{B}(\mathbf{s}) \cdot d\mathbf{s} = \text{RM}\lambda^2, \quad (2)$$

where $\Delta\chi$ is polarization angle offset due to Faraday rotation, $N(\mathbf{s})$ is the electron number density in cm^{-3} , $\mathbf{B}(\mathbf{s})$ is magnetic field in mG, and the integral is taken over a passage \mathbf{s} in parsec along the line of sight from the source to the observer, RM is the rotation measure in rad m^{-2} . The RM distribution can be used to explore the intervening plasma and magnetic field along the line of sight. To ensure proper estimation of RM, at least 3 band of EVPAs are required. Under the limitation of resolution and sensitivity for the current observational data, we cannot obtain a transverse RM variation across several beamwidths. Based on the resultant EVPAs between 15 and 43 GHz from model fitting, the components A and B are fitted with equation (2). As a result, the component A is badly fitted, while the EVPAs for the component B obeyed a λ^2 Faraday rotation law well, with the observed RM of $-1061.9 \pm 0.2 \text{ rad m}^{-2}$. The fitting result for both components is shown in Figure 6, where the errors are estimated from the Stokes Q and U images with 5σ of noise level adopted. In view of that the absolute RM due to our galaxy is usually no more than 200 rad m^{-2} in any direction (Pushkarev 2001), and the RM in the rest frame of NRAO 530 are higher by a factor of $(1+z)^2$, the RM in its rest frame will become quite large, with the absolute value of more than 3000 rad m^{-2} , which implies that most of the RM should arise from the source itself or plasma near the source, rather than the plasma in our galaxy.

Since there exists quite a large Faraday rotation for component B , it naturally reminds one that for the Faraday rotation occurring within the jet, radiation emitted at different depths is rotated through different angles, thus the net flux will be depolarized, and the polarization level will fall correspondingly. By contrast, external Faraday rotation is relatively hard to result in depolarization (e.g. Burn 1966). For an optically-thin uniform source, the internal Faraday dispersion can be described by an additional factor of $\sin(\Phi)/\Phi$ where $\Phi = 2.0\Delta\chi$ (Burn 1966; Homan et al. 2009). Based on the equation (2), the additional factors are obtained with values of 0.895, 0.975, and 0.998 at the corresponding frequency 15, 22, and 43 GHz, respectively. This means that even if all the observed rotation is completely in-

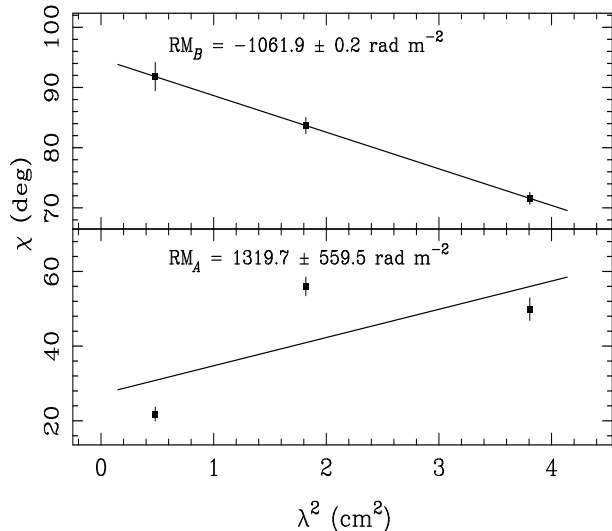


Figure 6. A λ^2 regression to the observed Faraday rotation as a solid line for component *A* (the bottom panel) and component *B* (the top panel). The uncertainties of RMs are derived assuming the reduced chi-square value of unity.

ternal to the jet, this rotation is not large enough to cause all of the decrease in fractional polarization observed, assuming that the component has comparable degree of polarization without depolarization. Homan et al. (2009) argued that the alternative cause inducing depolarization is the opacity by the mediums in the passage, by which the depolarization also gets worse with wavelength. This implies that both the opacity and internal Faraday rotation contribute to the decrease in fractional polarization with wavelength, in which the opacity plays quite a large part of role in the depolarization.

4 DISCUSSION

4.1 Core identification

In general, the core component in blazars lies in the extreme end of the jet, which is usually optically thick, and highly Doppler boosted with dominant flux density, relatively hard spectrum and high brightness temperature. By comparing the physical quantities of component *A* and *B* in Table 2, one can find that component *A* has higher brightness temperature and harder spectrum, both of which are indicators of radio core (e.g. Shen et al. 2005). On the other hand, the component *B* exhibits higher flux density and lower fractional polarization, which are also taken as the features of a radio core (e.g. Bower et al. 1997; Cotton et al. 1997). These apparently contrary observational evidences for core identification exists in both of the components, which increases the difficulty in core identification.

Due to large Doppler boosting effect present in NRAO 530 (Bower et al. 1997; Jorstad et al. 2001), it is impossible for the jet structure to be two-sided. Therefore, regardless of which one is the core component, the jet direction changes down the jet to connect the north-northwest structure (Jorstad et al. 2001). This will lead to changes of Doppler boosting effect down the jet. Assuming that the component *A* is the core of the object, the adverse condition

of relatively high fractional polarization and low flux density in core identification may be explained as follows: the component *B* has a relatively high flux density mainly due to the strong outburst occurring two years before (Jorstad et al. 2001), and possibly larger Doppler effect may also have contribution to it due to the change of jet viewing angle, which require further confirmation; as for its relatively high polarization level, it is because the component *A* itself consists at least two components (as is shown in the radio structure of higher resolution at 86 GHz (Bower et al. 1997)), of which the jet component enhances the overall fractional polarization of the fitted component *A*. For the same reason, the component *A* cannot be fitted well with a single power law spectrum (see Figure 3), and the EVPAs doesn't obey the wavelength square law as well (see Table 2) (Taylor 1998). If, on the contrary, the component *B* is the core, it is not only hard to explain its relatively soft spectrum, low brightness temperature, but also the trajectories are required to bend by nearly 180° to connect the north-northwest structure, which would be quite unnatural to interpret it logically. Combine all the above reasons, plus the component *A* lying in the south end of its radio structure, we conclude that it is the component *A* that is the true core of the object, which is consistent with the argument suggested in Jorstad et al. (2001) and Feng et al. (2006).

4.2 Magnetic geometry in jet

As mentioned earlier, the magnetic geometry is crucial in determining what role the magnetic field plays in the dynamics and emission of relativistic jets in active galactic nuclei, which may be helical due to the differential rotation of central engine (e.g. Meier, Koide & Uchida 2001), transverse due to shock compression, longitudinal due to the effect of shear or interaction with external medium (e.g. Laing 1980), or chaotic. Through polarimetric observations, the helical magnetic fields may manifest as spine-sheath polarization structure (the polarization electric vectors predominantly aligned with the jet in the jet spine and perpendicular to the jet at one or both edges) (e.g. Pushkarev et al. 2005), fractional polarization relatively low in the jet spine and increasing towards the jet edges (Lyutikov, Pariev & Gabuzda 2005)), and/or the exclusive feature of RM gradient across the jet (Blandford 1993; Asada et al. 2002).

4.2.1 Interpretation with magnetic compression and shear

As mentioned earlier, NRAO 530 shows the transverse *m* profile relatively low along the jet spine, and progressively increasing toward the jet edges, suggesting that the integrated magnetic field along the line of sight becomes better ordered toward the jet edges (Gómez et al. 2008). One possibility for presence of spine-sheath like structure as well as the magnetic bifurcate configuration might be related to the combination of shocks and flow shears (Laing 1980; Laing, Canvin & Bridle 2006). The shocks compress and partially order an initially tangled magnetic field, and the flow shear across the jet stretches the magnetic field along the jet (Wardle et al. 1994). The combination of shock compressions and flow velocity gradient across the jet may well reproduce the magnetic bifurcate configuration and the spine-sheath like *m* profiles (e.g. Laing 1980;

Laing, Canvin & Bridle 2006), which is found in the m and polarization structure of NRAO 530.

Another important observational feature for magnetic shock compression in AGNs is that the magnetic field projected on the sky plane is transverse to the local jet axis. This is because the relativistic shocks enhance the magnetic component in the plane of compression, perpendicular to the direction of propagation of the shock (Laing 1980; Hughes, Aller & Aller 1989). From the polarization structures at 5 and 8 GHz, the overall magnetic field directions in the bottom and top regions are roughly perpendicular to the local jet directions, which agrees well with the shock compression model. Furthermore, for the top two regions with detectable linear polarization at 5 GHz, one can find that the largest variation in fractional polarization appears to be North to South, where the polarization goes to zero between the two regions. The highest levels of fractional polarization are at the top (north) and bottom (south). It is likely that these two regions belong to a bigger bright shocked one, where the roughly transverse shocked field has canceled a roughly longitudinal field in the underlying jet. This will produce the effect that the middle of the structure appears to have the lowest polarization due to cancelation, as is predicted by shock in jet models (e.g. Gabuzda & Gómez 2001; Homan et al. 2009). Similar cases were also reported in some other sources (e.g. Gabuzda & Gómez 2001) with alternating aligned and orthogonal polarization vectors down the jet, where the longitudinal magnetic field mainly ascribed to the flow shear, oblique or conical shocks.

4.2.2 Helical interpretation of the magnetic configuration

It is also possible that the emission occurs in a large scale of helical magnetic field with certain combinations of pitch and viewing angle, resulting in the spine-sheath like m profiles in NRAO 530. For example, similar m profiles across the jet are presented with the viewing angle of $1/\Gamma$ or $1/2\Gamma$ in the observer's frame and pitch angle of 45° in the rest frame shown in Figure 9 in Lyutikov, Pariev & Gabuzda (2005) (here Γ is Lorentz factor). The extremely high fractional polarization at 5 and 8 GHz in the outmost emission region from the core might also be a manifestation of such a structure.

In addition, about 5 mas away from the core at 5 and 8 GHz, the polarization vectors bifurcate obviously to opposite sides from the local jet axis, something like a spine-sheath structure. At distances of 12 and 25 mas from the core at 5 GHz, such a structure can also roughly be seen, though it is not very obvious. Synchrotron emission of relativistic particles in a helical magnetic field can naturally explain the polarization structure in the jet frame (e.g. Pushkarev et al. 2005).

One may have noticed that the polarimetric properties of the object available for the current observations can not exclusively make it clear the magnetic configuration over the whole structure. Through multi-bands polarimetric VLBI observations of 3C 279 with the same 3 fitted components available at all the 6 bands from 8 to 22 GHz, Homan et al. (2009) obtained a self-consistent picture for its magnetic configuration, particle population and low cutoff energy range by numerical simulations to the full polarization spectra, which cannot be achieved in our case due mainly to the

limitation of the observational data and partly to the source structure itself. Additionally, at the 15 GHz and higher frequencies, the polarization structure is not resolvable over the jet width, which prevent us getting the transverse RM variation down the jet for further analysis on the magnetic configuration. It is noticeable that large orientation changes of polarization structure down the jet have also been detected in PKS 1418+546 and OJ287 (Gabuzda & Gómez 2001; Gabuzda & Chernetskii 2003). They both show a spine-sheath like structure in fractional polarization at the same time. This probably implies that there exists a certain connection between spine-sheath like structure and large orientation change of electric vectors down the jet, which is worthy of further investigation.

5 SUMMARY

We have performed the polarization-sensitive VLBI observations at 5, 8, 15, 22, and 43 GHz within a week in February 1997. Total intensity, fractional polarization, linear intensity and EVPA distributions at all these frequencies are presented. Model fitting has been done to the full polarimetric visibility data at all the 5 frequencies, with focus mainly on the two components A and B in the core region. Comparing to the component B , the southmost component A shows relatively high brightness temperature, hard spectrum, which is identified as the radio core of the object. The relatively high polarization level for the component is probably because it contains an additional jet component of high fractional polarization, which is resolved at 86 GHz with a VLBI observation of higher resolution (Bower et al. 1997). Whereas the component B of dominant flux density exhibits a good power-law spectrum with steady increase in fractional polarization with frequency from 15 to 43 GHz. The observed EVPAs for the component B is in agreement well with the λ^2 law, with the observed RM of about -1062 rad m^{-2} . Assuming that the component has a comparable degree of polarization without depolarization at these frequencies, both the opacity and internal Faraday rotation have effects on the decrease in fractional polarization with wavelength, in which the opacity plays quite a large part of role.

The linear polarization shows a spine-sheath like structure in some regions at 5 and 8 GHz with degree of polarization relatively low along the jet spine, but getting higher towards both edges. The largest variation in fractional polarization appears to be north to south, where the polarization goes to zero between the top two regions. The highest levels of fractional polarization occur at the bottom and top, while the lowest one occurs in the middle. The polarization structure at 5 GHz shows that the magnetic fields appear alternately orthogonal and aligned down the jet, with a signature of bifurcating to the opposite sides from the local jet spine. All these radiative features can be explained either with a large scale of helical magnetic field present within the jet, or with tangled magnetic fields compressed and sheared down the jet. Further polarimetric VLBI observations are required with sufficient high resolution and sensitivity at multiple wavelengths to further determine if the magnetic field is helical or not.

ACKNOWLEDGMENTS

The authors do appreciate the anonymous referee for insightful comments and constructive suggestions, which were greatly helpful in improving our paper, we also thank Prof. Jiang for helpful discussions. This work was supported by the National Natural Science Foundation of China (grants 10573029, 10625314, 10633010 and 10821302) and the Knowledge Innovation Program of the Chinese Academy of Sciences (Grant No. KJCX2-YW-T03), by the Science and Technology Commission of Shanghai Municipality (09ZR1437400) and the Scientific Research Foundation for Returned Scholars, Ministry of Education of China (9020090306), by the Program of Shanghai Subject Chief Scientist (06XD14024) and the National Key Basic Research Development Program of China (No. 2007CB815405). This paper made use of data from the University of Michigan Radio Astronomy Observatory, supported by the University of Michigan and the National Science Foundation. ZQS acknowledges the support by the One-Hundred-Talent Program of Chinese Academy of Sciences.

REFERENCES

- Asada K., Inoue M., Uchida Y., Kamenno S., Fujisawa K., Iguchi S., Mutoh M., 2002, PASJ, 54, L39
- Begelman M. C., Blandford R. D., Rees M. J., 1984, Rev. Mod. Phys., 56, 255
- Blandford R.D. 1993, Astrophysical Jets, Cambridge Univ. Press, Cambridge
- Bower G. C., Backer D. C., Wright M., Forster, J. R., 1997, ApJ, 484, 118
- Burn B.J., 1966, MNRAS, 133, 67
- Cotton W. D., Dallacasa D., Fanti C., Fanti R., Foley A. R., Schilizzi R. T., Spencer R. E. 1997, A&A, 325, 493
- Feng S.-W, Shen Z.-Q, Cai H.-B., Chen X., Lu R.-S., Huang L., 2006, A&A, 456, 97
- Gabuzda D.C., Gómez J.L., 2001, MNRAS, 320, L49
- Gabuzda D.C., Murray É., Cronin P., 2004, MNRAS, 351, L89
- Gabuzda D.C., & Chernetskii V.A., 2003, MNRAS, 339, 669
- Ghisellini G., Padovani P., Celotti A., Maraschi L., 1993, ApJ, 407, 65
- Gómez J.L., Marscher A.P., Jorstad S.G., Agudo I., Oca-Sogorb M., 2008, ApJ, 681, L69
- Homan d.C., Lister M.L., Aller H.D., Aller M.F., Wardle F.C., 2009, ApJ, 696, 328
- Hughes P.A., Aller H.D., Aller M.A., 1989, ApJ, 341, 68
- Jorstad S. G., Marscher A. P., Mattox J. R., Wehrle E., Bloom S. D., Yurchenko, A. V. 2001, ApJS, 134, 181
- Jorstad S.G. et al., 2007, ApJ, 134, 799
- Laing R., 1980, MNRAS, 193, 439
- Laing R. A., Canvin J. R., Bridle A. H., 2006, Astron. Nachr., 327, 523
- Lister M.L. et al., 2003, ApJ, 584, 135
- Lister M.L. et al., 2009, AJ, 138, 1874
- Lyutikov M., Pariev V.I., & Gabuzda D.C., 2005, MNRAS, 360, 869
- McKinney J.C., 2006, MNRAS, 367, 1797
- Meier D.L., Koide S., Uchida Y., 2001, Sci, 291, 84
- Pushkarev A.B., 2001, Astron. Rep., 45(9), 667
- Pushkarev A.B., Gabuzda D.C., Vetukhnovskaya Yu.N., Yakimov V.E., 2005, MNRAS, 859, 871
- Pyatunina T.B., Kudryavtseva N.A., Gabuzda D.C., Jorstad S.G., Aller M.F., Aller H.D., & Teräsranta H., 2006, MNRAS, 373, 1470
- Shen Z.-Q., et al., 2005, ApJ, 622, 811
- Taylor G.B., 1998, ApJ, 506, 637
- Wardle J. F. C., Cawthorne T. V., Roberts D. H., Brown L. F., 1994, ApJ, 437, 122
- Zavala R.T., Taylor G.B., 2004, ApJ, 612, 749
- Zavala R.T., Taylor G.B., 2005, ApJ, 626, L73